Spontaneous spherical symmetry breaking of black holes with resonant hair

José Ferreira,[1,*] Carlos A. R. Herdeiro,[1,†] Eugen Radu,[1,‡] and Miguel Zilhão[2,§]

[1] *Departamento de Matemática da Universidade de Aveiro and Centre for Research and Development in Mathematics and Applications (CIDMA), Campus de Santiago, 3810-193 Aveiro, Portugal*

[2] *Departamento de Física da Universidade de Aveiro and Centre for Research and Development in Mathematics and Applications (CIDMA), Campus de Santiago, 3810-193 Aveiro, Portugal*

(Dated: April 2026)

Black holes with resonant hair are static, spherical, electrically charged solutions of the Einstein-Maxwell-(gauged-)scalar system. Scalar self-interactions are mandatory for their existence. Initial dynamical studies restricted to spherical symmetry suggested stability; more recently, fully non-spherical dynamical studies revealed instabilities, at least for a particular class of self-interactions. Here, we provide a more detailed study of this instability together with a different decay channel, depending on the chosen solutions. Moreover, considering a second model, we provide evidence that the instabilities may be generic for different classes of self-interactions. We conclude these solutions are dynamically unstable and split into a bosonic lump and a bald black hole (via fission) or implode to the latter (via absorption). In both cases, the non-spherical dynamics seems to be key.

arXiv:2604.22437v2 [gr-qc] 30 Jun 2026

I. INTRODUCTION

Since the initial detections of gravitational waves (GWs) in 2015 [1], four observation catalogs have been released, totaling over 200 GW events [2–5]. In the coming years, the detection rate is anticipated to increase substantially, with both improvements to current detectors but also due to forthcoming next generation observatories such as Laser Interferometer Space Antenna (LISA) [6] and the Einstein Telescope. These advancements in GW astronomy will enable more precise tests of General Relativity (GR) and the nature of compact objects.

Simultaneously, advances in Numerical Relativity have allowed for the creation of larger and increasingly more accurate catalogs of numerically generated waveforms [7–10]. Notably, these catalogs are generated exclusively from the merger of Kerr Black Holes (BHs). Although these have been in good agreement with observations so far, to probe possible deviations from the Kerr paradigm, it becomes imperative to include waveforms from alternative models to future catalogs. A pioneering effort in this direction has been reported and used in [11, 12].

Several uniqueness theorems constrain the properties of BHs. However, these theorems can be evaded in multiple ways and create what are known as hairy BH solutions – see *e.g.* [13]. Nevertheless, for any such object to serve as a viable alternative to the Kerr BH, stability over astrophysically relevant timescales is required.

A notable example is BHs with resonant scalar hair [14]. These are static, spherically symmetric solutions to the Einstein-Maxwell-Scalar (EMS) model with a self-interacting, gauged, and minimally coupled scalar field. Recent nonlinear evolutions indicate that these solutions can be dynamically stable in spherical symmetry [15, 16], and can form via non-linear interaction with a charged scalar field [15].

This work investigates the nonlinear evolution of BHs endowed with resonant scalar hair beyond spherical symmetry, in 3+1 numerical relativity, evolving different configurations and exploring the possible end states, following up on the work [17]. The main conclusion is that these solutions are unstable, when non-spherical dynamics is taken into account. Moreover, we unveil a different decay channel from the one described in [17], show that the results are similar for different types of scalar potentials and conduct an analysis of the decay timescales for the unstable configurations.

The structure of this paper is as follows. Section II introduces the EMS model, details the equations of motion, and describes the 3+1 decomposition. In section III we outline the procedure for constructing initial data and the properties of representative configurations across the parameter space. Section IV presents the numerical setup and an analysis of the results. Final remarks and perspectives are provided in section V. Two appendices provide further technical details.

II. MODEL

A. Action and Field Equations

We consider an EMS model described by the Lagrangian density

$$\mathcal{L} = \frac{R}{16\pi} - \frac{1}{4}F_{\alpha\beta}F^{\alpha\beta} - (\widetilde{\nabla}_\alpha\phi)^*\widetilde{\nabla}^\alpha\phi - V(|\phi|)\,, \qquad (1)$$

where R denotes the Ricci scalar, $F_{\mu\nu} \equiv \nabla_\mu A_\nu - \nabla_\nu A_\mu$ is the Maxwell tensor, A_μ is the electromagnetic four-potential, ϕ is the complex scalar field, and $V(|\phi|)$ its potential. The (minimal) coupling between the scalar and the electromagnetic field is introduced via the gauge

* jpmferreira@ua.pt
† herdeiro@ua.pt
‡ eugen.radu@ua.pt
§ mzilhao@ua.pt

covariant derivative

$$\widetilde{\nabla}_\mu \phi \equiv \nabla_\mu \phi + iqA_\mu \phi \,, \tag{2}$$

where q is the coupling constant.

Variation of the action with respect to the metric yields the Einstein field equations

$$R_{\mu\nu} - \frac{1}{2} g_{\mu\nu} R = 8\pi \left(T^{\rm EM}_{\mu\nu} + T^{\phi}_{\mu\nu} \right) \,, \tag{3}$$

where $T^{\rm EM}_{\mu\nu}$ and $T^{\phi}_{\mu\nu}$ are the energy-momentum tensors for the electromagnetic and scalar field, respectively, given by

$$T^{\rm EM}_{\mu\nu} = F_\mu{}^\alpha F_{\nu\alpha} - \frac{1}{4} g_{\mu\nu} F_{\alpha\beta} F^{\alpha\beta} \,, \tag{4a}$$

$$T^{\phi}_{\mu\nu} = 2\widetilde{\nabla}_{(\mu} \phi^* \widetilde{\nabla}_{\nu)} \phi + g_{\mu\nu} \left[\widetilde{\nabla}^\alpha \phi^* \widetilde{\nabla}_\alpha \phi + V(|\phi|) \right] \,. \tag{4b}$$

Variation with respect to the electromagnetic potential leads to the Maxwell equations

$$\nabla_\alpha F^{\mu\alpha} = j^\mu \,, \tag{5}$$

where the electromagnetic current sourced by the scalar field is

$$j^\mu = iq \left[(\widetilde{\nabla}^\mu \phi)^* \phi - \phi^* (\widetilde{\nabla}^\mu \phi) \right] \,. \tag{6}$$

Variation with respect to the scalar field yields

$$\widetilde{\nabla}_\alpha \widetilde{\nabla}^\alpha \phi = \frac{dV}{d\,|\phi|^2} \phi \,. \tag{7}$$

We consider two different choices for $V(|\phi|)$: (i) a Q-ball type potential

$$V(|\phi|) = \mu^2 |\phi|^2 (1 - 2\lambda |\phi|^2)^2 \,, \tag{8}$$

where μ is the mass term and λ a self-interaction parameter; (ii) the axionic potential

$$V(|\phi|) = \frac{2\mu^2 f^2}{B} \left(1 - \sqrt{1 - 4B \sin\left(\frac{|\phi|}{2f} \right)} \right) \,, \tag{9}$$

where f and B are free parameters, with $4|B| \leqslant 1$.

B. Cauchy problem formulation

To solve the previous equations numerically, we rewrite them using the $3+1$ decomposition [18, 19]. The spacetime line element is written as[1]

$$ds^2 = -\alpha^2 dt^2 + \gamma_{ij} (dx^i + \beta^i dt)(dx^j + \beta^j dt) \,, \tag{10}$$

where α is the lapse, β^i is the shift vector and $\gamma_{\mu\nu}$ is the induced metric on the spatial hypersurface, defined as

$$\gamma_{\mu\nu} \equiv g_{\mu\nu} + n_\mu n_\nu \,, \tag{11}$$

with $n_\mu = (-\alpha, 0, 0, 0)$ the future-directed unit normal vector.

The electromagnetic four-potential is decomposed into spatial and normal components,

$$A_\mu = \mathcal{A}_\mu + A_\phi n_\mu \,, \tag{12}$$

where $\mathcal{A}_\alpha \equiv \gamma_\alpha{}^\beta A_\beta$ and $A_\phi \equiv -n^\alpha A_\alpha$. The Maxwell tensor becomes

$$F_{\mu\nu} = D_\mu \mathcal{A}_\nu - D_\nu \mathcal{A}_\mu + n_\mu E_\nu - n_\nu E_\mu \,, \tag{13}$$

where $E^\mu \equiv \gamma^{\mu\alpha} n^\beta F_{\alpha\beta}$ is the electric field, and D_i is the covariant derivative compatible with γ_{ij}, defined generically as

$$D_i T^{\mu_1 \ldots \mu_n}{}_{\nu_1 \ldots \nu_n} \equiv \gamma^{\mu_1}{}_{\alpha_1} \ldots \gamma^{\mu_n}{}_{\alpha_n} \gamma^{\beta_1}{}_{\nu_1} \ldots \gamma^{\beta_n}{}_{\nu_n} \gamma^\rho{}_i \nabla_\rho T^{\alpha_1 \ldots \alpha_n}{}_{\beta_1 \ldots \beta_n} \,. \tag{14}$$

Contracting the first index of eq. (13) with n_μ and projecting the second index with $\gamma^\nu{}_\beta$ yields the evolution equation for $\mathcal{A}^i$,

$$\partial_t \mathcal{A}^i = -\alpha E^i - D^i (A_\phi \alpha) + \beta^j D_j \mathcal{A}^i - \mathcal{A}^j D_j \beta^i \,. \tag{15}$$

Substituting eq. (13) into eq. (5), the normal projection gives the constraint

$$M \equiv D_i E^i - 4\pi \rho_e = 0 \,, \tag{16}$$

where $\rho_e \equiv -n_\mu j^\mu$ is the normal component of the four-current. The spatial projection yields the evolution equation

$$\begin{aligned} \partial_t E^i = {} & \alpha K E^i + \beta^j D_j E^i - E^j D_j \beta^i \\ & + D_j (\alpha (D^i \mathcal{A}^j - D^j \mathcal{A}^i)) - \alpha z^i \,, \end{aligned} \tag{17}$$

where $z^i \equiv \gamma^i{}_k j^k$ is the spatial projection of j^μ, and $K \equiv \gamma^{ij} K_{ij}$ is the trace of the extrinsic curvature. The $3+1$ decomposition of the current yields

$$\rho_e = -2iq (\phi K^*_\phi - \phi^* K_\phi) - 2q^2 A_\phi \phi \phi^* \,, \tag{18a}$$

$$z^i = -2iq \left(\phi \partial^i \phi^* - \phi^* \partial^i \phi \right) - 2q^2 \mathcal{A}^i \phi \phi^* \,, \tag{18b}$$

where the conjugate momentum of the scalar field K_ϕ is defined as

$$K_\phi \equiv -\frac{1}{2} n^\alpha \nabla_\alpha \phi \,. \tag{19}$$

The Lorenz gauge condition, $\nabla_\mu A^\mu = 0$, is imposed to fix the electromagnetic gauge freedom, leading to the evolution equation for A_ϕ,

$$\partial_t A_\phi = \beta^i \partial_i A_\phi + \alpha K A_\phi - \alpha D_j \mathcal{A}^j - \mathcal{A}^j \partial_j \alpha \,. \tag{20}$$

[1] Greek indices denote four-dimensional quantities, while Latin indices refer to three-dimensional spatial components.

To control violations of the constraint eq. (16), the equations of motion are modified following the approach of [20, 21], introducing an auxiliary variable Z and a constraint damping parameter κ. The modified equations read

$$\partial_t E^i = \alpha K E^i + \beta^j D_j E^i - E^j D_j \beta^i + D_j(\alpha(D^i \mathcal{A}^j - D^j \mathcal{A}^i)) + \alpha D^i Z - 4\pi\alpha z^i \,, \tag{21a}$$

$$\partial_t A_\phi = \beta^i \partial_i A_\phi + \alpha K A_\phi - \alpha D_j \mathcal{A}^j - \mathcal{A}^j \partial_j \alpha - \alpha Z \,. \tag{21b}$$

with the auxiliary variable Z evolving as

$$\partial_t Z = \alpha M - \alpha\kappa Z + \beta^j \partial_j Z \,. \tag{22}$$

For the scalar field, a first-order reduction is performed,

$$\nabla_\mu \phi = D_\mu \phi + 2K_\phi n_\mu \,, \tag{23}$$

where K_ϕ is taken as an independent variable. Rewriting eq. (19) we obtain the time derivative for the scalar field

$$\partial_t \phi = \beta^j \partial_j \phi - 2\alpha K_\phi \,. \tag{24}$$

Substituting eq. (19) into eq. (7) gives the evolution equation for K_ϕ,

$$\partial_t K_\phi = \alpha K K_\phi + \beta^j \partial_j K_\phi - \frac{1}{2} D^i(\alpha \partial_i \phi) + \frac{1}{2}\alpha \frac{dV}{d\,|\phi|^2}\phi - i\alpha q \left(\mathcal{A}^i \partial_i \phi - 2K_\phi A_\phi\right) + \frac{\alpha q^2}{2}\left(\mathcal{A}^i \mathcal{A}_i - A_\phi^2\right)\phi \,, \tag{25}$$

C. Physical Quantities

The minimal coupling between the scalar and electromagnetic fields means the scalar field is electrically charged. A quantum of scalar field has charge q. The total charge of a BH-scalar field system can then be decomposed as [14]

$$Q = Q_h + Q_\phi \,, \tag{26}$$

where Q_ϕ is the total charge associated with the scalar field and Q_h is the charge associated with the horizon region. In the $3+1$ formalism, the scalar field charge is computed as

$$Q_\phi = \frac{1}{4\pi}\int_{r_h}^{\infty} \sqrt{\gamma}\rho_e \, d^3x \,, \tag{27}$$

where γ is the determinant of the spatial metric and ρ_e is the normal projection of the electromagnetic current defined above. r_h is the radial coordinate of the BH horizon.

As for the BH charge, Q_h, it is defined via a surface integral at the horizon,

$$Q_h = -\frac{1}{4\pi}\oint_{\mathcal{H}} \sqrt{\gamma^{(2)}} F^{\mu\nu} n_\mu \sigma_\nu \, d^2x \,, \tag{28}$$

where $\gamma^{(2)}$ is the determinant of the induced two-metric on the horizon $\mathcal{H}$, n_μ is the future-directed unit normal to the hypersurface, and σ_ν is the outward-pointing normal to the horizon surface. To avoid computing surface integrals, we determine the value of Q_h by computing the total charge Q (as explained next) and using eq. (26).

To evaluate the total charge and the outgoing electromagnetic radiation, we make use of the Newman–Penrose scalars defined as [22]

$$\Phi_1 \equiv \frac{1}{2} F_{\mu\nu}\left(l^\mu k^\nu + \bar{m}^\mu m^\nu\right) \,, \tag{29a}$$

$$\Phi_2 \equiv F_{\mu\nu} \bar{m}^\mu k^\nu \,, \tag{29b}$$

where l, k and m are constructed from an orthonormal triad u, v, w orthogonal to n^μ according to

$$l^\alpha = \frac{1}{\sqrt{2}}\left(n^\alpha + u^\alpha\right) \,, \tag{30a}$$

$$k^\alpha = \frac{1}{\sqrt{2}}\left(n^\alpha - u^\alpha\right) \,, \tag{30b}$$

$$m^\alpha = \frac{1}{\sqrt{2}}\left(v^\alpha + i w^\alpha\right) \,. \tag{30c}$$

At sufficiently large coordinate radius $R_{\rm ex}$ the scalars are decomposed in spin-weighted spherical harmonics

$$\Phi_1 = \sum_{l,m} \phi_1^{lm}(t) Y^0_{lm} \,, \tag{31a}$$

$$\Phi_2 = \sum_{l,m} \phi_2^{lm}(t) Y^{-1}_{lm} \,, \tag{31b}$$

which, for outgoing waves in the far-field regime, are related to the components of the electric and magnetic fields as [23]

$$\Phi_1 \approx \frac{1}{2}\left(E_{\hat{r}} + iB_{\hat{r}}\right) \,, \tag{32a}$$

$$\Phi_2 \approx E_{\hat{\theta}} - iE_{\hat{\varphi}} \,. \tag{32b}$$

For a non rotating, point-like, charged particle in flat spacetime, the only non-zero component of the electric field is

$$E_{\hat{r}} = \frac{Q}{r^2} \,, \tag{33}$$

which when inserted in eq. (31a) yields, at the extraction radius,

$$\phi_1^{00} = \frac{\sqrt{\pi} Q}{R_{\rm ex}^2} \,, \tag{34}$$

allowing the extraction of the total charge Q from the measured ϕ_1^{00} at the chosen extraction radius.

III. INITIAL DATA

The initial data considered in this work corresponds to asymptotically flat, spherically symmetric BHs with resonant scalar hair in the model (1). This type of solutions has been previously constructed and analyzed in [14, 24, 25]. Here, the procedure for generating such solutions is briefly summarized and further technical details can be found in the cited references.

The scalar field and the electromagnetic 4-potential are assumed to take the form

$$\phi = \Phi(r)e^{-i\omega t}\,, \qquad A = U(r)dt\,, \tag{35}$$

where $\Phi(r)$ denotes the radial profile of the scalar field, ω is its (real) oscillation frequency, and $U(r)$ is the electric potential. Throughout this section, r denotes the isotropic radial coordinate.

To describe a spherically symmetric spacetime, the following metric ansatz in isotropic coordinates is adopted:

$$ds^2 = -e^{2\mathcal{F}_0}\frac{S_0^2}{S_1^2}dt^2 + e^{2\mathcal{F}_1}S_1^4 d\Sigma^2\,, \tag{36}$$

where $d\Sigma^2$ is the line element of three-dimensional flat space, and $\mathcal{F}_0(r)$ and $\mathcal{F}_1(r)$ are undetermined functions. The auxiliary functions S_0 and S_1 are defined as

$$S_0 \equiv 1 - \frac{r_h}{r}\,, \qquad S_1 \equiv 1 + \frac{r_h}{r}\,, \tag{37}$$

with r_h representing the horizon radius of the BH.

Regularity of the energy-momentum tensor at the horizon imposes the resonance condition

$$\omega = qU(r_h)\,. \tag{38}$$

Imposing that the electric potential vanishes at spatial infinity, the bound-state condition for the scalar field yields an upper bound on the frequency,

$$\omega \leq \mu\,. \tag{39}$$

These conditions are derived under the assumption that the gauge is chosen such that the electric potential $U(r)$ vanishes at spatial infinity.

Substituting the ansatz eqs. (35) and (36) into the Einstein field equations, together with the matter sector equations, results in a system of ordinary differential equations for the four functions $\mathcal{F}_0(r)$, $\mathcal{F}_1(r)$, $\Phi(r)$, and $U(r)$. For a given model, specified by the parameters q and μ, λ (for the potential eq. (8)) or μ, f, B (for the potential eq. (9)), solutions are obtained by varying the ansatz parameters ω and r_h.

As in boson stars, a notable feature of the solution space is the existence of distinct branches for fixed values of ω and r_h. In this case we have an upper and a lower branch. The existence curves in the (M_T, ω) plane for the Q-ball potential eq. (8), for several values of r_h, are displayed in fig. 1, where M_T denotes the total mass of the system. A qualitatively similar plot is valid for the axionic potential eq. (9).

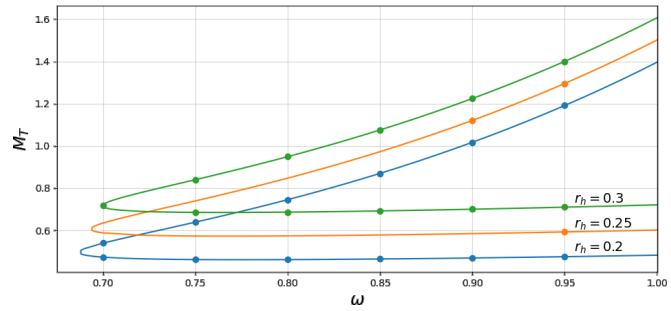

FIG. 1. Solution curves for the Q-ball potential with $\mu = 1$, $\lambda = 2500$, and $q = 12$. M_T is the total mass of the system. Dots indicate solutions that are evolved in the next section.

Qualitatively, the upper branch solutions are characterized by less compact configurations, with the scalar hair extending further from the BH. Along this branch, increasing ω leads to an increase in the spatial extent of the hair. In contrast, the lower branch exhibits the opposite behavior: increasing ω results in more compact configurations. This is illustrated in fig. 2, which shows the density profile of the scalar field as a function of r for representative values of ω belonging to both branches. The picture is qualitatively the same when considering the Q-ball potential.

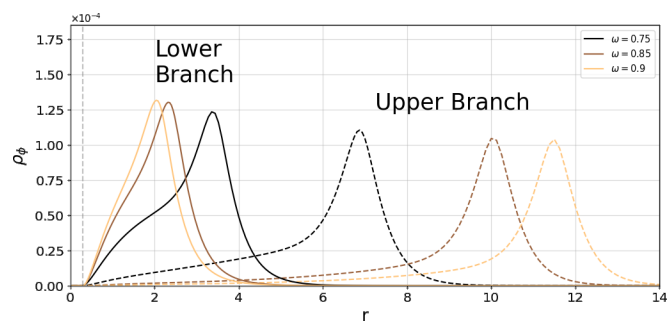

FIG. 2. Radial profile of the scalar field density ρ_ϕ versus radius r for solutions with $r_h = 0.2$ and three different values of ω for the axionic potential. For the lower branch (solid lines), increasing ω increases the compactness of the hair, while for the upper branch (dashed lines), the compactness decreases.

For future reference, we note that the hair compactness does not vary significantly when fixing ω and varying r_h, along the lower branches.

IV. RESULTS

A. Numerical Setup

The evolutions are performed in units where the mass of the scalar field is set to $\mu = 1$. For the Q-ball poten-

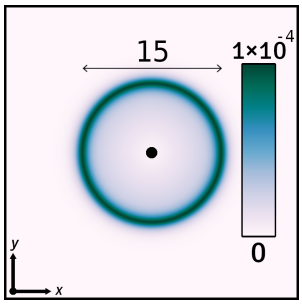

(a) Initial configuration

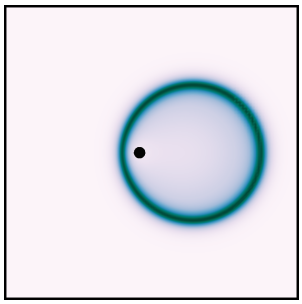

(b) Instability develops

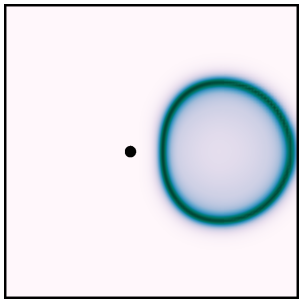

(c) BH is expelled by the hair

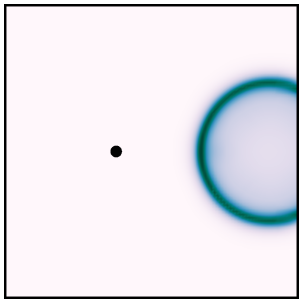

(d) Final state, BS plus BH

FIG. 3. Snapshots of the normal density of the scalar field with axionic potential in the xy plane for *fission*, with $r_h = 0.3$ and $\omega = 0.75$ in the upper branch. The final state is a stable BS and a hairless BH with opposite momenta.

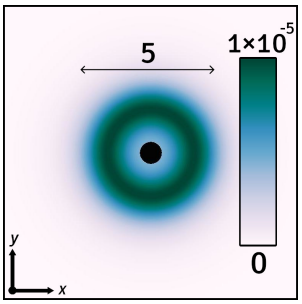

(a) Initial configuration

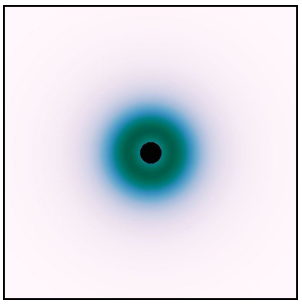

(b) Instability develops

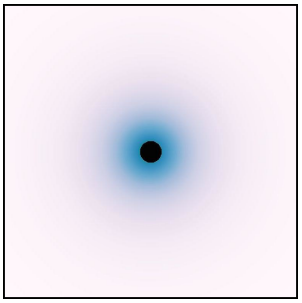

(c) Hair is getting absorbed

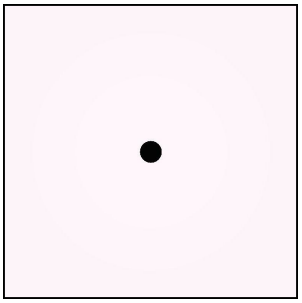

(d) Final state, a hairless BH

FIG. 4. Snapshots of the normal density of the scalar field with Q-Ball potential in the xy plane for *absorption*, with $r_h = 0.2$ and $\omega = 0.95$ in the lower branch. The final state is characterized by a hairless BH.

tial we consider $\lambda = 2500$ [2] and $q = 12$. For the axionic case, we set $B = 0.22$, $f = 0.01$ and $q = 3$. We explored the parameter space region $0.2 \leq r_h \leq 0.3$ and ω ranging from 0.7 to 0.95 in increments of 0.05. The results presented in this section correspond to a representative subset of the simulations that were performed.

Time evolutions are performed using the Einstein Toolkit [26, 27], employing the `MagnetoScalar` thorn [28], the Carpet mesh refinement infrastructure [29], horizon tracking via `AHFinderDirect` [30], and metric evolution with BSSN [31, 32] using the thorn `LeanBSSNMoL` [33, 34].

The simulations are performed on a $256 \times 256 \times 128$ grid with reflection symmetry imposed on the xy plane. A box-in-a-box mesh refinement strategy with nine levels is employed, with a grid spacing of $h = 4$ on the coarsest mesh. The grid dynamically tracks the puncture location of the BH during the evolution. Kreiss-Oliger dissipation is implemented using the "continuous" scheme described in [35]. Spatial derivatives are computed using fourth-order finite differences, and time integration is carried out with a fourth-order Runge-Kutta method.

For the outer boundaries, we impose radiative boundary conditions using the `NewRad` infrastructure. Due to the usage of puncture coordinates for the time evolution, the horizon of the BH does not require any special treatment.

Post-processing of the simulation data is performed with Kuibit [36] and Visit [37]. The analysis scripts and selected results are made publicly available in [38].

Details regarding the convergence of the numerical setup are provided in appendix B.

B. Time Evolutions

Evolving these solutions reveals two qualitatively distinct outcomes: (i) *absorption*, in which the hair is absorbed by the BH, and (ii) *fission*, already discussed in [17], where the BH is expelled from the hair resulting in a stable (charged) BS and a hairless (charged) BH. Representative snapshots of these decay mechanisms are displayed in fig. 3 for fission and fig. 4 for absorption.

The fate of each solution seems to be correlated with the compactness of the hair. Solutions with more compact hair, typically found in the lower branch at higher ω, undergo absorption. In contrast, less compact configurations, located in the upper branch or in the lower branch with smaller ω, exhibit the fission instability. We emphasize that these behaviors are universal for both potentials considered.

To quantitatively characterize the lifetime of each so-

[2] This large value of λ allows the contributions of the quartic/sextic terms in the potential to be of the same order as that of the mass term.

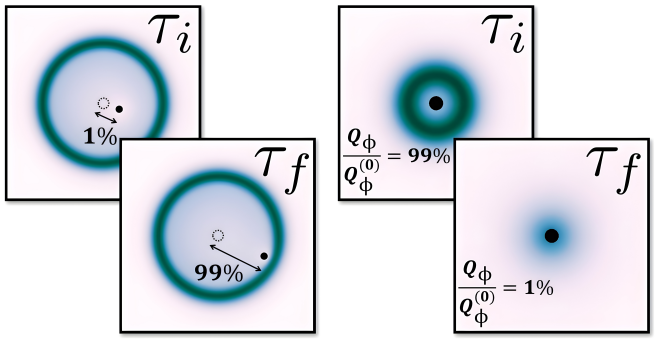

FIG. 5. Schematic representation of the definitions for τ_i and τ_f for *fission* (left) and for *absorption* (right).

lution, we define two instants of time, τ_i and τ_f, represented schematically for each decay mechanism in fig. 5. Additionally, we define the quantity $\Delta\tau \equiv \tau_f - \tau_i$, that we interpret as the timescale of the process.

For *fission*, we define a sphere of radius R_i as the sphere containing 1% of the total charge of the scalar field, and R_f as the radius of a sphere containing 99% of the total charge of the scalar field[3]. We define τ_i as the moment in time when the centroid of the BH crosses R_i, and τ_f as the time it crosses R_f.

As for *absorption*, τ_i is defined as the time when the charge of the scalar field Q_ϕ drops to 99% of its initial value, and τ_f as the time when Q_ϕ reaches 1% of its initial value.

We verified that using different values in the definition of τ_i and τ_f for either scenarios (e.g. 5% and 95% or 10% and 90%), does not qualitatively affect the conclusions. For more information, refer to appendix A.

Since we do not add any perturbation to our system, the only source of the instability is numerical noise. This means that, for the same physical system, but for different numerical setups (e.g. resolution, dissipation, etc.), the values of both τ_i and τ_f vary. However, the value of $\Delta\tau$ remains consistent across different numerical configurations. Because of this, our analysis will only focus on $\Delta\tau$, as it is the only physically meaningful timescale in this context.

In fig. 6, we present the timescale $\Delta\tau$ for the absorption process as a function of r_h, considering Q-ball potential and $\omega = 0.95$. Here, r_h is chosen as the reference parameter since the absorption instability is observed exclusively for solutions with more compact hair, typically found in the lower branch. For these cases, r_h is varied between solutions in the lower branch. The results show that $\Delta\tau$ decreases monotonically with increasing r_h, indicating that (compact hair) configurations with larger

[3] The radius of the spherical surface is evaluated at $t = 0$. Since the scalar hair remains approximately spherically symmetric until the centroid is expelled, this radius is treated as constant.

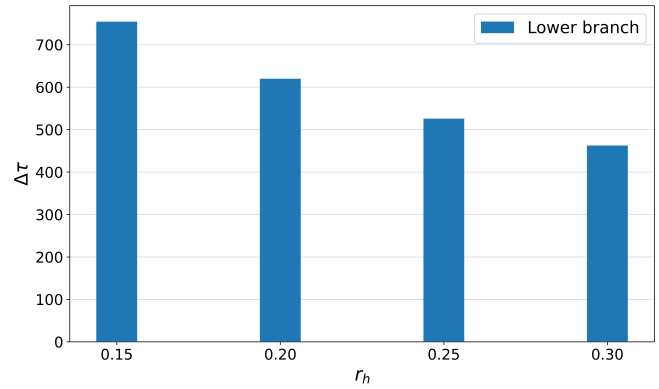

FIG. 6. The value of $\Delta\tau$ versus r_h for *absorption*, considering the Q-ball potential and $\omega = 0.95$. All solutions exhibiting this instability are in the lower branch.

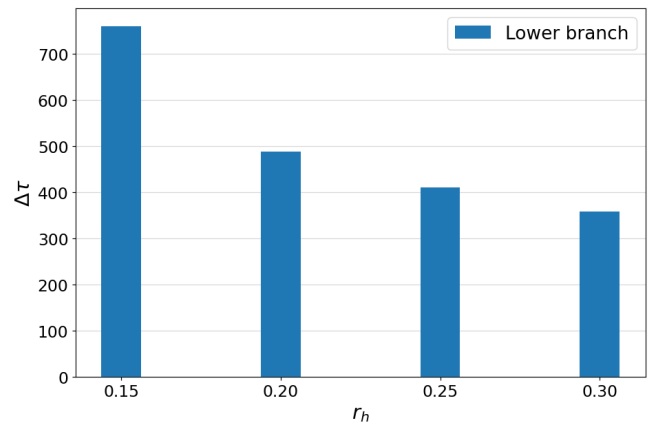

FIG. 7. The value of $\Delta\tau$ versus r_h for *absorption*, considering the axionic potential and $\omega = 0.95$. All solutions exhibiting this instability are in the lower branch.

BHs are more unstable (at fixed ω). For the axionic potential, presented in fig. 7, we observe the same behavior: increasing r_h decreases the value of $\Delta\tau$ monotonically.

In fig. 8 we present $\Delta\tau$ for the fission instability versus ω, assuming a Q-ball potential and fixing $r_h = 0.2$. We can see that $\Delta\tau$ increases with ω in the lower branch, showing that more compact solutions take longer to decay than less compact solutions. In the upper branch, $\Delta\tau$ exhibits a non-monotonic dependence on ω, reflecting the influence of additional parameters such as mass and charge for the stability of the configuration. For the axionic potential, fig. 9 demonstrates that the instability timescale $\Delta\tau$ exhibits minimal dependence on the frequency ω along the lower branch, whereas the upper branch displays non-monotonic behavior consistent with the results obtained considering the Q-ball potential.

In both potentials, we see a similar pattern: more compact solutions exhibit the absorption instability, while less compact solutions exhibit the fission instability. Notably, the values of $\Delta\tau$ are of the same order between

both potentials, indicating that the timescale of the instability is independent of the specific form of the scalar potential.

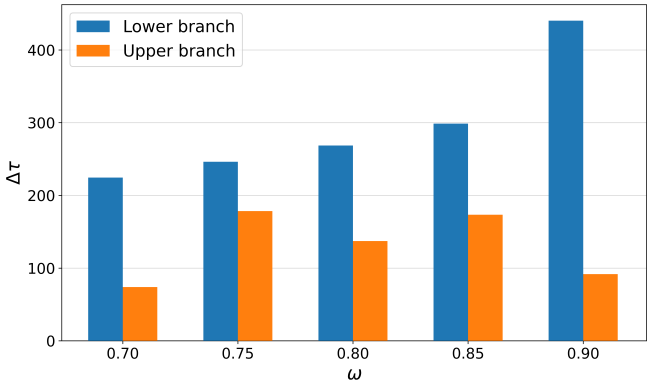

FIG. 8. The value of $\Delta\tau$ versus ω for *fission*, considering the Q-ball potential and $r_h = 0.2$.

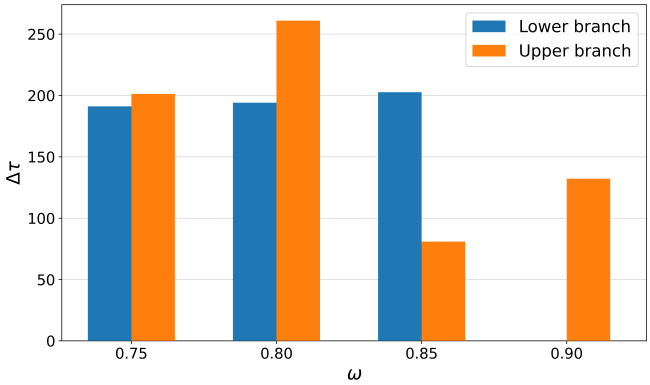

FIG. 9. The value of $\Delta\tau$ versus ω for *fission*, considering the axionic potential and $r_h = 0.3$.

V. FINAL REMARKS

In this work, we studied the stability of BHs with resonant hair using fully nonlinear $3+1$ numerical relativity simulations. Although previous work in spherical symmetry indicated stability, the present analysis has identified two distinct decay mechanisms arising from non-spherically symmetric instabilities: one in which the BH absorbs the surrounding hair, and another in which the BH is expelled from the scalar hair, leaving behind a stable BS. In both cases, the loss of spherical symmetry seems to be a key ingredient for the instability to develop.

It was observed that solutions with more compact hair tend to absorb the scalar field, whereas those with less compact configurations are more susceptible to the ejection of the BH. In some regions of parameter space, we found that the timescale of the decay was correlated with the compactness of the scalar hair. However, this correlation was not universal, and competing factors such as the mass and the charge of the hair and those of the BH also play a role in determining the timescale of the instability. A systematic exploration of the parameter space is required to better understand the dependence of the timescales of the instability.

These results indicate that the observed instabilities are generic properties of BHs with resonant hair[4]. This instability is caused by the unstable balance between gravitational pull and electromagnetic repulsion between the hair and the BH, which we expect to affect a wider region of parameter space and to be largely independent of the specific scalar potential.

ACKNOWLEDGMENTS

This work is supported by the Center for Research and Development in Mathematics and Applications (CIDMA) (https://ror.org/05pm2mw36) under the Portuguese Foundation for Science and Technology (FCT – Fundação para a Ciência e a Tecnologia, https://ror.org/00snfqn58), Grants UID/04106/2025 (https://doi.org/10.54499/UID/04106/2025) and UID/PRR/04106/2025 (https://doi.org/10.54499/UID/PRR/04106/2025), as well as the projects: Horizon Europe staff exchange (SE) programme HORIZON-MSCA2021-SE-01 Grant No. NewFunFiCO-101086251 and 2022.04560.PTDC (https://doi.org/10.54499/2022.04560.PTDC). J.F. is funded by FCT through project 2023.04333.BD (https://doi.org/10.54499/2023.04333.BD). The authors thankfully acknowledge computational resources from RES provided by BSC (MareNostrum) through projects FI-2024-2-0012, FI-2024-3-0007, POR021PROD, and by IFCA (Altamira) through project FI-2025-1-0011. Computational resources were also provided via FCT through projects 2025.09498.CPCA.A3, 2024.07872.CPCA.A2 (DOI: 10.54499/2024.07872.CPCA.A2 https://doi.org/10.54499/2024.07872.CPCA.A2) at Deucalion supercomputer, jointly funded by EuroHPC JU and Portugal, and at MareNostrum through project 2024.07059.CPCA.A3 (DOI: 10.54499/2024.07059.CPCA.A3 https://doi.org/10.54499/2024.07059.CPCA.A3).

Appendix A: Dependence of Timescales on Scalar Field Charge Threshold

We here investigate how the choice of thresholds for defining the timescales τ_i and τ_f affects the value of $\Delta\tau$.

[4] A process with some similarities has been observed in AdS for spherically symmetric black holes in [39].

We consider three different sets of thresholds: *(i)* 1% and 99%, *(ii)* 5% and 95%, and *(iii)* 10% and 90%. The results for the Q-ball potential are summarized in fig. 10, for the absorption scenario, and in fig. 11 for the fission scenario.

For the axionic potential, the results are presented in fig. 12 for the fission scenario and in fig. 13 for the absorption scenario.

As illustrated in the figures, the choice of thresholds does not change the qualitative behavior of $\Delta\tau$, as the trends observed in the main text remain consistent across different threshold values.

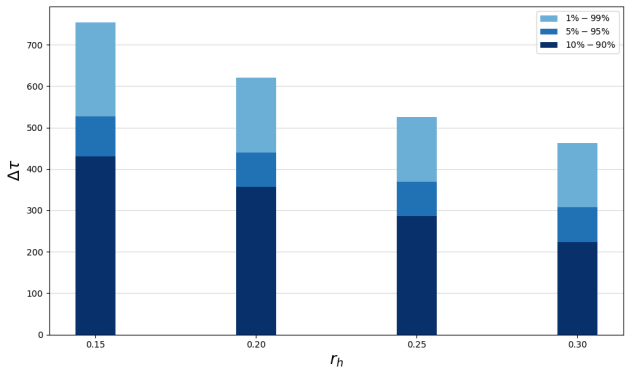

FIG. 10. Value of $\Delta\tau$ versus r_h for the *absorption* scenario in Q-ball potential with $\omega = 0.95$, for different thresholds. All solutions exhibiting this instability are in the lower branch.

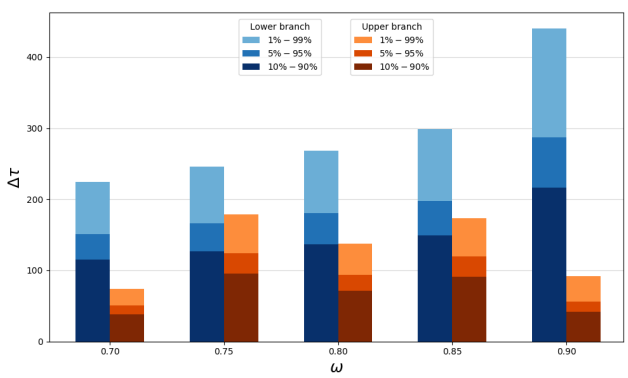

FIG. 11. Value of $\Delta\tau$ versus ω for the *fission* scenario in Q-ball potential with $r_h = 0.2$, for different thresholds.

Appendix B: Convergence

Here we present some convergence results that validate the numerical evolution. We monitor the Hamiltonian constraint

$$\mathcal{H} \equiv \mathcal{R} + K^2 - K_{ij}K^{ij} - 16\pi\rho\,, \tag{B1}$$

where $\mathcal{R}$ is the Ricci scalar of the spatial metric, $\rho \equiv n_a n_b T^{ab}$ is the normal energy density and K the trace of

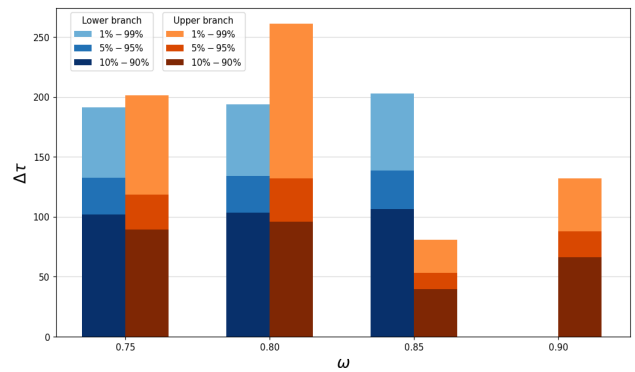

FIG. 12. Value of $\Delta\tau$ versus ω for the *fission* scenario in axionic potential with $r_h = 0.3$, for different thresholds.

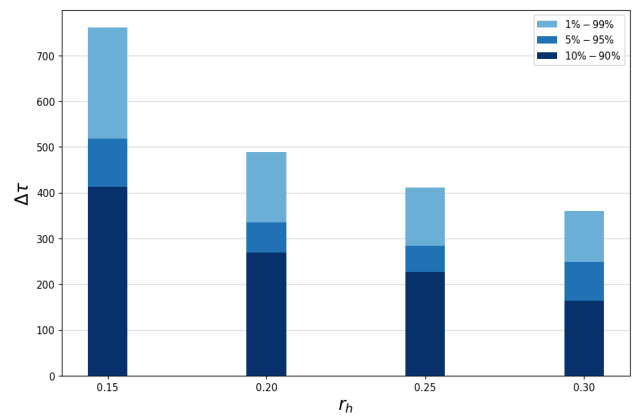

FIG. 13. Value of $\Delta\tau$ versus r_h for the *absorption* scenario in axionic potential with $\omega = 0.95$, for different thresholds.

the extrinsic curvature K_{ij} that is defined as

$$K_{ij} \equiv -D_i n_j\,. \tag{B2}$$

For the case of *absorption*, we run the same simulation with two different resolutions and perform a convergence analysis of the norm-2 of the Hamiltonian. We show that the norm-2 of the Hamiltonian constraint $\mathcal{H}$ exhibits second-order convergence to zero. This behavior is illustrated in fig. 14.

For *fission* we also observe second order convergence to zero of the norm-2 of the Hamiltonian constraint (left plot of fig. 15). Since instabilities are sourced by numerical noise, the time at which the BH starts moving, τ_i, differs between different resolutions. If we re-scale the time in this regime appropriately, we can see that the Hamiltonian constraint still converges with second order (right plot of fig. 15).

The convergence observed is second-order, consistent with the second-order prolongation operations used by Carpet. Fourth-order convergence is obtained at $t = 0$, however, as expected.

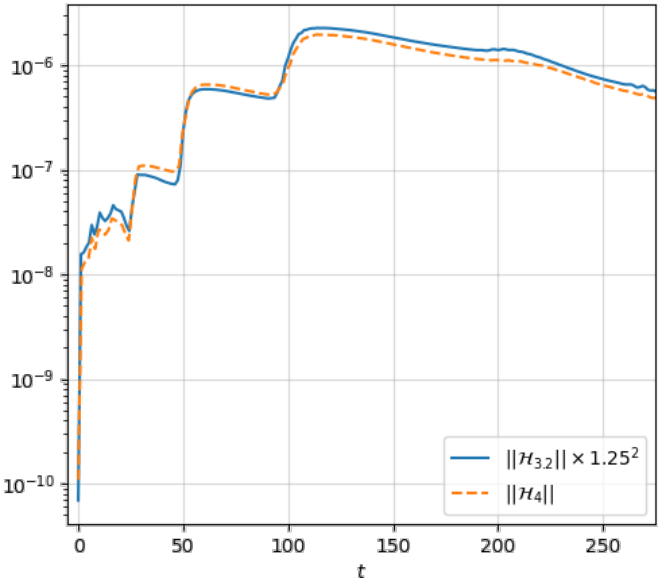

FIG. 14. Convergence to zero of the norm-2 of the Hamiltonian constraint $\mathcal{H}$ for Q-ball potential with $r_h = 0.3$ and $\omega = 0.95$, in the lower branch, corresponding to the absorption process.

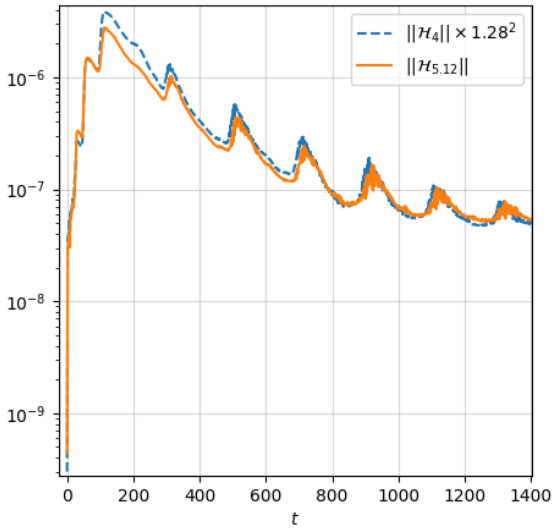

(a) Hamiltonian constraint $\mathcal{H}$ before fission takes place.

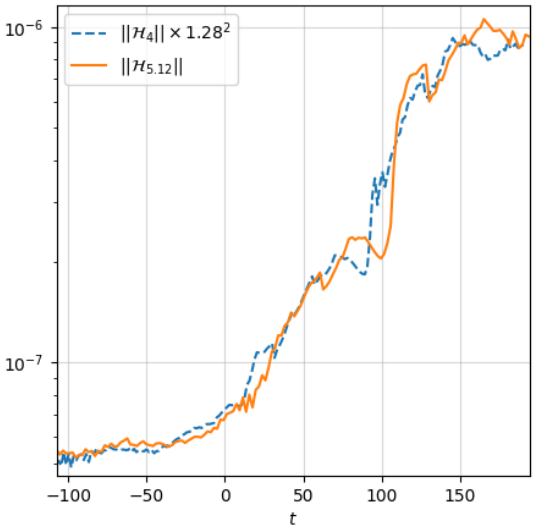

(b) Hamiltonian constraint $\mathcal{H}$ during the fission process.

FIG. 15. Convergence to zero of the norm-2 of the Hamiltonian constraint $\mathcal{H}$ for Q-ball potential with $r_h = 0.3$ and $\omega = 0.7$, in the upper branch. The plot on the right is time shifted to match the position of the punctures, such that $t = 0$ corresponds to the time the puncture leaves the region in which most of the hair is located.

[1] R. Abbott, Gw190521: A binary black hole merger with a total mass of 150 msun, Physical Review Letters **125**, 101102 (2020).

[2] R. Abbott, Gwtc-1: A gravitational-wave transient catalog of compact binary mergers observed by ligo and virgo during the first and second observing runs, Physical Review X **9**, 031040 (2019).

[3] R. Abbott, Gwtc-2: Compact binary coalescences ob-

served by ligo and virgo during the first half of the third observing run, Physical Review X **11**, 021053 (2021).

[4] R. Abbott, Gwtc-3: Compact binary coalescences observed by ligo and virgo during the second part of the third observing run, Physical Review X **13**, 041039 (2023).

[5] A. G. Abac *et al.* (LIGO Scientific, KAGRA, VIRGO), GWTC-4.0: An Introduction to Version 4.0 of the Gravitational-Wave Transient Catalog, Astrophys. J. Lett. **995**, L18 (2025), arXiv:2508.18080 [gr-qc].

[6] P. Amaro-Seoane, H. Audley, S. Babak, J. Baker, E. Barausse, P. Bender, E. Berti, P. Binetruy, M. Born, D. Bortoluzzi, J. Camp, C. Caprini, V. Cardoso, M. Colpi, J. Conklin, N. Cornish, C. Cutler, K. Danzmann, R. Dolesi, L. Ferraioli, V. Ferroni, E. Fitzsimons, J. Gair, L. G. Bote, D. Giardini, F. Gibert, C. Grimani, H. Halloin, G. Heinzel, T. Hertog, M. Hewitson, K. Holley-Bockelmann, D. Hollington, M. Hueller, H. Inchauspe, P. Jetzer, N. Karnesis, C. Killow, A. Klein, B. Klipstein, N. Korsakova, S. L. Larson, J. Livas, I. Lloro, N. Man, D. Mance, J. Martino, I. Mateos, K. McKenzie, S. T. McWilliams, C. Miller, G. Mueller, G. Nardini, G. Nelemans, M. Nofrarias, A. Petiteau, P. Pivato, E. Plagnol, E. Porter, J. Reiche, D. Robertson, N. Robertson, E. Rossi, G. Russano, B. Schutz, A. Sesana, D. Shoemaker, J. Slutsky, C. F. Sopuerta, T. Sumner, N. Tamanini, I. Thorpe, M. Troebs, M. Vallisneri, A. Vecchio, D. Vetrugno, S. Vitale, M. Volonteri, G. Wanner, H. Ward, P. Wass, W. Weber, J. Ziemer, and P. Zweifel, Laser interferometer space antenna 10.48550/arxiv.1702.00786 (2017), arXiv:1702.00786 [astro-ph.IM].

[7] J. Healy, C. O. Lousto, Y. Zlochower, and M. Campanelli, The rit binary black hole simulations catalog, Classical and Quantum Gravity **34**, 224001 (2017), arXiv:1703.03423 [gr-qc].

[8] M. Boyle, D. Hemberger, D. A. B. Iozzo, G. Lovelace, S. Ossokine, H. P. Pfeiffer, M. A. Scheel, L. C. Stein, C. J. Woodford, A. B. Zimmerman, N. Afshari, K. Barkett, J. Blackman, K. Chatziioannou, T. Chu, N. Demos, N. Deppe, S. E. Field, N. L. Fischer, E. Foley, H. Fong, A. Garcia, M. Giesler, F. Hebert, I. Hinder, R. Katebi, H. Khan, L. E. Kidder, P. Kumar, K. Kuper, H. Lim, M. Okounkova, T. Ramirez, S. Rodriguez, H. R. Rüter, P. Schmidt, B. Szilagyi, S. A. Teukolsky, V. Varma, and M. Walker, The sxs collaboration catalog of binary black hole simulations, Classical and Quantum Gravity **36**, 195006 (2019), arXiv:1904.04831 [gr-qc].

[9] K. Jani, J. Healy, J. A. Clark, L. London, P. Laguna, and D. Shoemaker, Georgia tech catalog of gravitational waveforms, Classical and Quantum Gravity **33**, 204001 (2016), arXiv:1605.03204 [gr-qc].

[10] I. Hinder, A. Buonanno, M. Boyle, Z. B. Etienne, J. Healy, N. K. Johnson-McDaniel, A. Nagar, H. Nakano, Y. Pan, H. P. Pfeiffer, M. Pürrer, C. Reisswig, M. A. Scheel, E. Schnetter, U. Sperhake, B. Szilágyi, W. Tichy, B. Wardell, A. Zenginoglu, D. Alic, S. Bernuzzi, T. Bode, B. Brügmann, L. T. Buchman, M. Campanelli, T. Chu, T. Damour, J. D. Grigsby, M. Hannam, R. Haas, D. A. Hemberger, S. Husa, L. E. Kidder, P. Laguna, L. London, G. Lovelace, C. O. Lousto, P. Marronetti, R. A. Matzner, P. Mösta, A. Mroué, D. Müller, B. C. Mundim, A. Nerozzi, V. Paschalidis, D. Pollney, G. Reifenberger, L. Rezzolla, S. L. Shapiro, D. Shoemaker, A. Taracchini, N. W. Taylor, S. A. Teukolsky, M. Thierfelder, H. Witek, and Y. Zlochower, Error-analysis and comparison to analytical models of numerical waveforms produced by the nrar collaboration, Class. Quantum Grav. 31 (2014) 025012 **31**, 025012 (2013), arXiv:1307.5307 [gr-qc].

[11] J. C. Bustillo, N. Sanchis-Gual, A. Torres-Forné, J. A. Font, A. Vajpeyi, R. Smith, C. Herdeiro, E. Radu, and S. H. W. Leong, GW190521 as a merger of Proca stars: A potential new vector boson of 8.7×10^{-13} ev, Physical Review Letters **126**, 081101 (2021).

[12] N. Sanchis-Gual, J. Calderón Bustillo, C. Herdeiro, E. Radu, J. A. Font, S. H. W. Leong, and A. Torres-Forné, Impact of the wavelike nature of Proca stars on their gravitational-wave emission, Phys. Rev. D **106**, 124011 (2022), arXiv:2208.11717 [gr-qc].

[13] C. A. R. Herdeiro and E. Radu, Asymptotically flat black holes with scalar hair: A review, International Journal of Modern Physics D **24**, 1542014 (2015).

[14] C. A. R. Herdeiro and E. Radu, Spherical electro-vacuum black holes with resonant, scalar q-hair, The European Physical Journal C **80**, 10.1140/epjc/s10052-020-7976-9 (2020), arXiv:2004.00336 [gr-qc].

[15] C.-Y. Zhang, Q. Chen, Y. Liu, Y. Tian, B. Wang, and H. Zhang, Nonlinear self-interaction induced black hole bomb 10.48550/ARXIV.2309.05045 (2023), arXiv:2309.05045 [gr-qc].

[16] L. Zhao, L. Chen, and C.-Y. Zhang, Radial oscillations of scalar hair in black hole bombs 10.48550/ARXIV.2508.15477 (2025), arXiv:2508.15477 [gr-qc].

[17] J. Nicoules, J. Ferreira, C. A. R. Herdeiro, E. Radu, and M. Zilhão, Splitting the gravitational atom: Instabilities of black holes with synchronized or resonant hair, Phys. Rev. D **113**, L061507 (2026), arXiv:2509.20450 [gr-qc].

[18] T. W. Baumgarte, *Numerical Relativity: Solving Einstein's Equations on the Computer* (Cambridge University Press, 2010) p. 698.

[19] M. Alcubierre, J. C. Degollado, and M. Salgado, The einstein-maxwell system in 3+1 form and initial data for multiple charged black holes, Physical Review D **80**, 104022 (2009), arXiv:0907.1151 [gr-qc].

[20] M. Zilhão, H. Witek, and V. Cardoso, Nonlinear interactions between black holes and proca fields, Classical and Quantum Gravity **32**, 234003 (2015), arXiv:1505.00797 [gr-qc].

[21] D. Hilditch, An introduction to well-posedness and free-evolution, International Journal of Modern Physics A Vol. 28 (2013) 1340015 **28**, 1340015 (2013), arXiv:1309.2012 [gr-qc].

[22] E. Newman and R. Penrose, An approach to gravitational radiation by a method of spin coefficients, Journal of Mathematical Physics **3**, 566 (1962).

[23] M. Zilhão, V. Cardoso, C. Herdeiro, L. Lehner, and U. Sperhake, Collisions of charged black holes, Phys. Rev. D 85, 124062 (2012) **85**, 124062 (2012), arXiv:1205.1063 [gr-qc].

[24] J.-P. Hong, M. Suzuki, and M. Yamada, Charged black holes in non-linear q-clouds with o(3) symmetry, Physics Letters B **803**, 135324 (2020).

[25] J.-P. Hong, M. Suzuki, and M. Yamada, Spherically symmetric scalar hair for charged black holes, Physical Review Letters **125**, 111104 (2020).

[26] L. Werneck, S. Cupp, T. Assumpção, S. R. Brandt, C.-

H. Cheng, P. Diener, J. Doherty, Z. Etienne, R. Haas, T. P. Jacques, B. Karakaş, K. Topolski, B.-J. Tsao, M. Alcubierre, D. Alic, G. Allen, M. Ansorg, M. Babiuc-Hamilton, L. Baiotti, W. Benger, E. Bentivegna, S. Bernuzzi, T. Bode, G. Bozzola, B. Brendal, B. Bruegmann, M. Campanelli, F. Cipolletta, G. Corvino, R. D. Pietri, A. Dima, H. Dimmelmeier, R. Dooley, N. Dorband, M. Elley, Y. E. Khamra, J. Faber, G. Ficarra, T. Font, J. Frieben, B. Giacomazzo, T. Goodale, C. Gundlach, I. Hawke, S. Hawley, I. Hinder, E. A. Huerta, S. Husa, T. Ikeda, S. Iyer, L. Ji, D. Johnson, A. V. Joshi, H. Kalyanaraman, A. Kankani, W. Kastaun, T. Kellermann, A. Knapp, M. Koppitz, N. Kuo, P. Laguna, G. Lanferman, P. Lasky, L. Leung, F. Löffler, H. Macpherson, J. Masso, L. Menger, A. Merzky, J. M. Miller, M. Miller, P. Moesta, P. Montero, B. Mundim, P. Nelson, A. Nerozzi, S. C. Noble, C. Ott, L. J. Papenfort, R. Paruchuri, D. Pollney, D. Price, D. Radice, T. Radke, C. Reisswig, L. Rezzolla, C. B. Richards, D. Rideout, M. Ripeanu, L. Sala, J. A. Schewtschenko, E. Schnetter, B. Schutz, E. Seidel, E. Seidel, J. Shalf, K. Sible, U. Sperhake, N. Stergioulas, W.-M. Suen, B. Szilagyi, R. Takahashi, M. Thomas, J. Thornburg, C. Tian, M. Tobias, A. Tonita, S. Tootle, P. Walker, M.-B. Wan, B. Wardell, A. Wen, H. Witek, M. Zilhão, B. Zink, and Y. Zlochower, The einstein toolkit (2023).

[27] M. Zilhão and F. Löffler, An Introduction to the Einstein Toolkit, Int. J. Mod. Phys. A **28**, 1340014 (2013), arXiv:1305.5299 [gr-qc].

[28] V. Jaramillo, D. Núñez, M. Ruiz, and M. Zilhão, Full 3D nonlinear dynamics of charged and magnetized boson stars, Phys. Rev. D **111**, 024070 (2025), arXiv:2411.07284 [gr-qc].

[29] E. Schnetter, S. H. Hawley, and I. Hawke, Evolutions in 3-D numerical relativity using fixed mesh refinement, Class. Quantum Grav. **21**, 1465 (2004), arXiv:gr-qc/0310042.

[30] J. Thornburg, A Fast Apparent-Horizon Finder for 3-Dimensional Cartesian Grids in Numerical Relativity, Class. Quantum Grav. **21**, 743 (2004), arXiv:gr-qc/0306056.

[31] T. W. Baumgarte and S. L. Shapiro, Numerical integration of einstein's field equations, Physical Review D **59**, 024007 (1998).

[32] M. Shibata and T. Nakamura, Evolution of three-dimensional gravitational waves: Harmonic slicing case, Physical Review D **52**, 5428 (1995).

[33] H. Witek, M. Zilhao, G. Ficarra, and M. Elley, Canuda: a public numerical relativity library to probe fundamental physics (2020).

[34] U. Sperhake, Binary black-hole evolutions of excision and puncture data, Phys. Rev. D **76**, 104015 (2007), arXiv:gr-qc/0606079.

[35] G. Bozzola and V. Paschalidis, Numerical-relativity simulations of the quasi-circular inspiral and merger of non-spinning, charged black holes: methods and comparison with approximate approaches, Phys. Rev. D 104, 044004 (2021) **104**, 044004 (2021), arXiv:2104.06978 [gr-qc].

[36] G. Bozzola, kuibit: Analyzing Einstein Toolkit simulations with Python, J. Open Source Softw. **6**, 3099 (2021), arXiv:2104.06376 [gr-qc].

[37] H. Childs, E. Brugger, B. Whitlock, J. Meredith, S. Ahern, D. Pugmire, K. Biagas, M. C. Miller, C. Harrison, G. H. Weber, H. Krishnan, T. Fogal, A. Sanderson, C. Garth, E. W. Bethel, D. Camp, O. Rubel, M. Durant, J. M. Favre, and P. Navratil, High Performance Visualization–Enabling Extreme-Scale Scientific Insight (2012).

[38] https://github.com/jpmvferreira/instability-QhairyBH/.

[39] Z. Ning, Q. Chen, Y. Tian, X. Wu, and H. Zhang, Spontaneous deformation of an ads spherical black hole, Phys. Rev. D **109**, 064082 (2024).